Title
Dynamic Control of Optical Response in Layered Metal Chalcogenide Nanoplates

Journal
Nano Letters, 16(1)

ISSN
1530-6984

Authors
Liu, Yanping
Tom, Kyle
Wang, Xi
et al.

Publication Date
2016-01-13

DOI
10.1021/acs.nanolett.5b04140

Peer reviewed

NANO LETTERS

Letter

pubs.acs.org/NanoLett

Dynamic Control of Optical Response in Layered Metal Chalcogenide Nanoplates

Yanping Liu,[†] Kyle Tom,[†,‡] Xi Wang,[†] Chunming Huang,[†] Hongtao Yuan,[§,∥] Hong Ding,[⊥] Changhyun Ko,[†] Joonki Suh,[†] Lawrence Pan,[†] Kristin A. Persson,[†,⊥] and Jie Yao*[,†,‡]

[†]Department of Materials Science and Engineering, University of California, Berkeley, California 94720, United States

[‡]Materials Sciences Division and [⊥]Environmental Energy Technologies Division, Lawrence Berkeley National Laboratory, Berkeley, California 94720, United States

[§]Geballe Laboratory for Advanced Materials, Stanford University, Stanford, California 94305, United States

[∥]Stanford Institute for Materials and Energy Sciences, SLAC National Accelerator Laboratory, Menlo Park, California 94025, United States

S *Supporting Information*

ABSTRACT: Tunable optical transitions in ultrathin layered 2-dimensional (2D) materials unveil the electronic structures of materials and provide exciting prospects for potential applications in optics and photonics. Here, we present our realization of dynamic optical modulation of layered metal chalcogenide nanoplates using ionic liquid (IL) gating over a wide spectral range. The IL gating significantly increased the tuning range of the Fermi level and, as a result, substantially altered the optical transitions in the nanoplates. Using heavily n-doped Bi_2Se_3 nanoplates, we substantially modulated the light transmission through the ultrathin layer. A tunable, high-transmission spectral window in the visible to near-infrared region has been observed due to simultaneous shifts of both the plasma edge and absorption edge of the material. On the other hand, optical response of multilayer $MoSe_2$ flakes gated by IL has shown enhanced transmission in both positive and negative biases, which is consistent with their ambipolar electrical behavior. The electrically controlled optical property tuning in metal chalcogenide material systems provides new opportunities for potential applications, such as wide spectral range optical modulators, optical filters, and electrically controlled smart windows with extremely low material consumption.

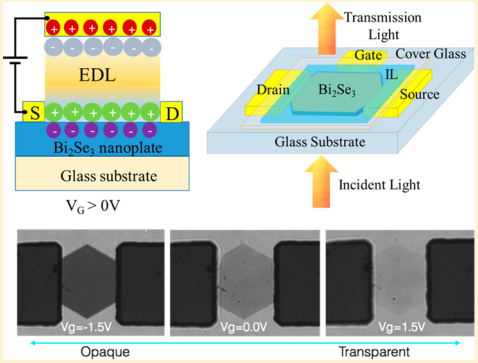

KEYWORDS: *Dynamic optical tuning, 2D materials, metal chalcogenides, ionic liquid gating*

The emergence of two-dimensional (2D) layered structure materials beyond graphene have opened new scenarios in the exploration of low-dimensional electronic systems.[1−6] These materials, such as hexagonal-boron nitride (h-BN)[7,8] and transition metal dichalcogenides (TMDCs),[9−14] are formed from weak van der Waals interaction between layers and strong covalent bonding within each layer. The rich spectrum of properties in 2D layered structure crystals has created exciting prospects for potential applications in valleytronics,[15−18] nonlinear optics, sensing,[19,20] and transparent electrodes.[21,22] Bismuth selenide (Bi_2Se_3), one of these layered 2D materials, has been shown to be a topological insulator (TI), characterized by its band insulator behavior in the bulk and gapless linear energy dispersion relationship at the sample boundary that is a result of unbroken time-reversal symmetry.[23−27] Recently, some research groups have reported that the optoelectronic properties in Bi_2Se_3 can be modified via bulk doping,[28] intercalation,[29−31] and surface deposits.[32,33] The dramatic changes in Bi_2Se_3 optical properties have attracted particular interest in this material system. However, such processes have to be done in the material preparation stage, and the material's optical properties cannot be changed once an optical device has been made. Dynamic electrical control of the optical properties of layered metal chalcogenides in the visible spectrum has not been reported yet. This is attributed to the difficulty of tuning the Fermi level and carrier density of the chalcogenides over a wide range via traditional electrical gating approaches. To overcome these obstacles, we employed an electric-double-layer (EDL) gating technique at room temperature to dynamically tune the optical properties in layered structure materials from infrared to visible wavelengths. The dynamic optical modulation induced by the EDL gating can be used in potential applications that would not be suitable for the intercalation technique, including wide spectral range optical modulators and large-area electrically controlled smart windows. Since the gating technique is electrically controlled, the devices can easily be controlled using a light sensor and a battery source.

Received: October 11, 2015
Revised: November 13, 2015
Published: November 24, 2015

DOI: 10.1021/acs.nanolett.5b04140
Nano Lett. 2016, 16, 488−496

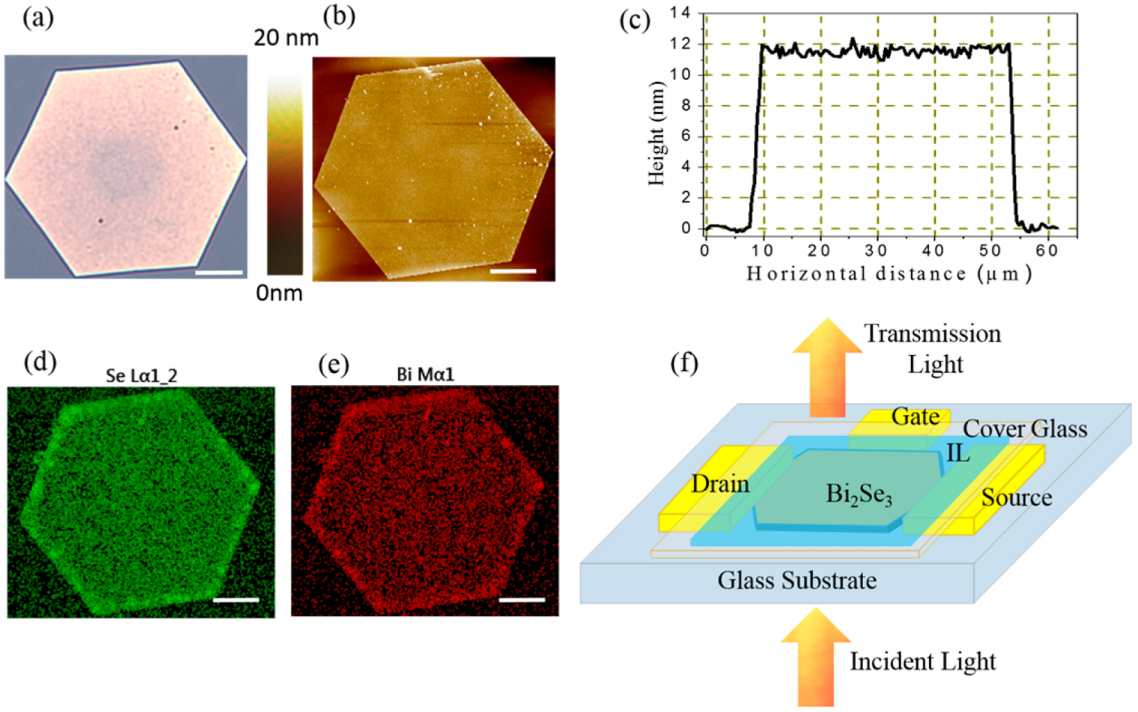

Figure 1. Bi_2Se_3 nanoplates and device schematic. (a) Optical image of the Bi_2Se_3 nanoplates on a glass substrate. (b) Atomic force microscopy (AFM) image of the Bi_2Se_3 nanoplates. (c) Line profile across the AFM image in c, which shows a clear value of around 12 nm for the nanoplate thickness. SEM-EDS mapping of Se (d) and Bi (e) element distribution in Bi_2Se_3 nanoplates. Scale bar, 10 μm. (f) Sketch of optical device configuration using EDL for gate modulation. A gate voltage is applied between a gold gate electrode and the Bi_2Se_3 nanoplates. The arrow indicates the propagation direction of light though the device.

EDL gating using ionic liquids (ILs) as the gate dielectric has been shown to substantially tune the electronic states and the Fermi energy (E_F) of semiconductors.[34,35] Compared to using oxide dielectrics, this technique offers lower-power and larger carrier concentration tuning.[35,36] When a gate voltage (V_G) is applied to the electrodes, an electric double layer (EDL) is generated at the liquid/solid interface after the ionic redistribution, creating a huge capacitance caused by nanogap capacitors. The capacitance of the EDLs exceeds 10 $\mu F/cm^2$,[37] meaning that it can accumulate or deplete larger quantities of charge carriers at the surface of the sample more effectively than an oxide dielectric FET under the same V_G. This improvement can lead to advancements in electrostatic modulation of interfacial electronic states, such as electric-field-induced superconductivity in ZrNCl and $SrTiO_3$.[38] The unprecedented gating power of ionic liquids enabled us to realize dynamic enhancement and reduction of optical transmission through Bi_2Se_3 nanoplates by applying positive and negative gate voltages, respectively, which will be shown in the following sections. Similar dynamic tuning of optical properties was also observed in other layered-structured TMDC materials, such as $MoSe_2$. The lightly doped $MoSe_2$, in contrast to the Bi_2Se_3, shows an optical tuning behavior regardless of the sign of the gate voltage, which is consistent with its ambipolar electrical properties. Our observation indicates that the IL gating (ILG) technique not only provides a powerful method for modulating the electronic transport and other physical properties in materials such as Bi_2Se_3, but also simplifies device fabrication and reduces energy consumption. The unique EDL gating mechanism based on ion migration and EDL formation allows the gate electrode to be far away from the gated material, which completely removes the light-blocking metal gate that would normally be above the material in traditional gate conurations and provides great advantages for optical measurements and photonic device designs.

Results. *Material Preparation and Characterization.* Bi_2Se_3 nanoplates were synthesized using solvothermal synthesis[29,39] with details provided in the Methods section. The thickness of the nanoplates range from several to tens of nanometers. Their lateral dimensions may go up to 80 μm, which is larger than other reported results for solvothermal synthesis and provides a good platform for studying optical properties. An optical image of a typical Bi_2Se_3 nanoplate on a Si/SiO_2 (300 nm) substrate is shown in Figure 1a. The lateral size of the nanoplate is around 50 μm. Its thickness was measured using atomic force microscopy (AFM) as shown in Figure 1b. Figure 1c shows a line profile of the nanoplate from Figure 1 b and indicates that the thickness of the nanoplate is around 11 nm. AFM results of multiple nanoplates with different thicknesses were shown in Supplementary Figure S1. To confirm the identity of the grown nanoplates, we carried out Raman spectroscopy (Supplementary Figure.S2). The three clear characteristic peaks located at ~71 cm^{-1}, ~131 cm^{-1}, and ~173 cm^{-1} are in excellent agreement with the reported Raman spectrum of Bi_2Se_3.[40] To better identify the elements of the Bi_2Se_3 nanoplates, scanning electron microscope- energy dispersive X-ray spectroscopy (SEM-EDS) element mapping of Bi_2Se_3 nanoplates was performed and is shown in Figure 1d (Se) and Figure 1e (Bi). The electron diffraction results (shown in Figure S3b)) further demonstrate the single crystalline nature of the nanoplates.

To study the optical modulation in Bi_2Se_3 nanoplates controlled with EDL gating, optical spectral measurements were carried out to characterize individual nanoplates with and

DOI: 10.1021/acs.nanolett.5b04140
Nano Lett. 2016, 16, 488−496

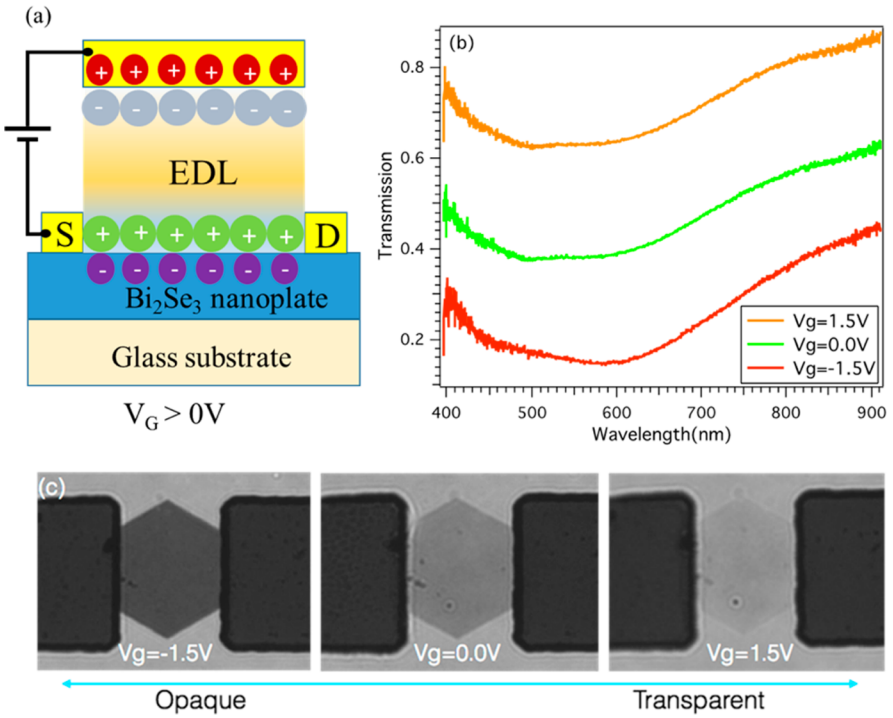

Figure 2. Visible transparency modulation of Bi_2Se_3 nanoplates using EDLG. (a) Schematic diagram of electron accumulation in EDLTs. The electric double-layer transistor geometry was operated by using the IL for gate modulation. The electric charge accumulation results in an electric field at the interface, which can be used to tune the density of electrons in the surface-electron-accumulation layer at the surface of the Bi_2Se_3 samples. (b) Optical transmission spectra of Bi_2Se_3 nanoplates between 400 and 900 nm under the applied EDL gate voltage. The transmission spectra show a higher transmission value at long wavelengths than at shorter wavelengths. The spectra elucidate the widening and lessening of the optical bandgap after the applied positive and negative EDL gate voltage. (c) Optical transmission images of the Bi_2Se_3 nanoplates with thickness around 15 nm under the applied EDL gating. The observed results clearly demonstrate optical modulation behavior in layered structure Bi_2Se_3 nanoplates via EDL gating.

without ILG. Figure 1f shows a sketch of the device configuration using EDL for gate modulation. A voltage is applied between a gold gate electrode and the Bi_2Se_3 nanoplate. The cover glass is used to ensure uniform EDL thickness to reduce lensing effects and effects from liquid motion after application. The arrow indicates the propagation direction of light through the device. The IL utilized in this experiment was *N*-diethyl-*N*-(2-methoxyethyl)-*N*-methylammonium bis-(trifluoromethylsulfonyl)-imide ([DEME]-[TFSI]), an imidazolium-based compound which exhibits rather high ionic conductivity and is widely used in EDL devices. It has a very wide transparent window from visible to mid-IR, which covers the complete frequency range of interest. We have placed a droplet of IL on both a gold electrode and a Bi_2Se_3 nanoplate with an electrode attached to generate the Au/IL/Bi_2Se_3/Au configuration shown in Figure 1d. The device dimensions between source and drain electrodes are W = 50 μm in width and L = 30 μm in length. The entire device is completely covered by the IL droplet. Applying the IL as the dielectric for EDL transistors (EDLTs) on the surface of the Bi_2Se_3 nanoplates subsequently allows us to dynamically modulate its electronic states and E_F. Figure 2a shows a schematic diagram of the electron accumulation case in Bi_2Se_3 nanoplates. As shown in Figure 2a, when a positive gate voltage is applied, electrons will accumulate at the nanoplate's interface with the IL. An EDL will then form at the interface, and the corresponding Fermi level will rise. A negative gate voltage, on the other hand, will lower the Fermi level in the gated material.

EDL gating impacts the optical response of Bi_2Se_3 profoundly even in the visible frequency range. Figure 2b shows the transmission spectra of Bi_2Se_3 nanoplates with and without EDL gating between 400 and 900 nm. Without an applied gate voltage, the optical transmission is relatively low for the device, about 40%. In contrast, the transmission increases dramatically for all visible wavelengths when positive gate voltages are applied. For example, at a gate voltage of 1.5 V, the transmission increases to around 70% in most of the visible range, meaning that Bi_2Se_3 nanoplates become much more transparent. On the other hand, when a negative gate voltage is applied, the Bi_2Se_3 nanoplates become highly opaque. The transmission decreases to around 20% in most of the visible range after applying a gate voltage of −1.5 V. Figure 2c shows transmission mode optical images of Bi_2Se_3 nanoplates under the applied ILG with thicknesses around 15 nm. The observed results clearly demonstrate the optical modulation behavior in Bi_2Se_3 nanoplates via ILG. Moreover, the transmission increases as the wavelength becomes longer (Figure 2b). Such a trend continues all the way to near-infrared wavelengths, providing a clear signature of an absorption edge. Below, we provide more experimental evidence to elucidate the mechanism of the drastic optical modulation behavior in metal chalcogenide nanoplates with EDL gating.

Analysis and Discussion. A key feature of this work is that the free carriers induced by the EDL gating modify the conductivity of the materials, which also significantly alters their optical properties. Figure 3a and b shows the transmission and

DOI: 10.1021/acs.nanolett.5b04140
Nano Lett. 2016, 16, 488−496

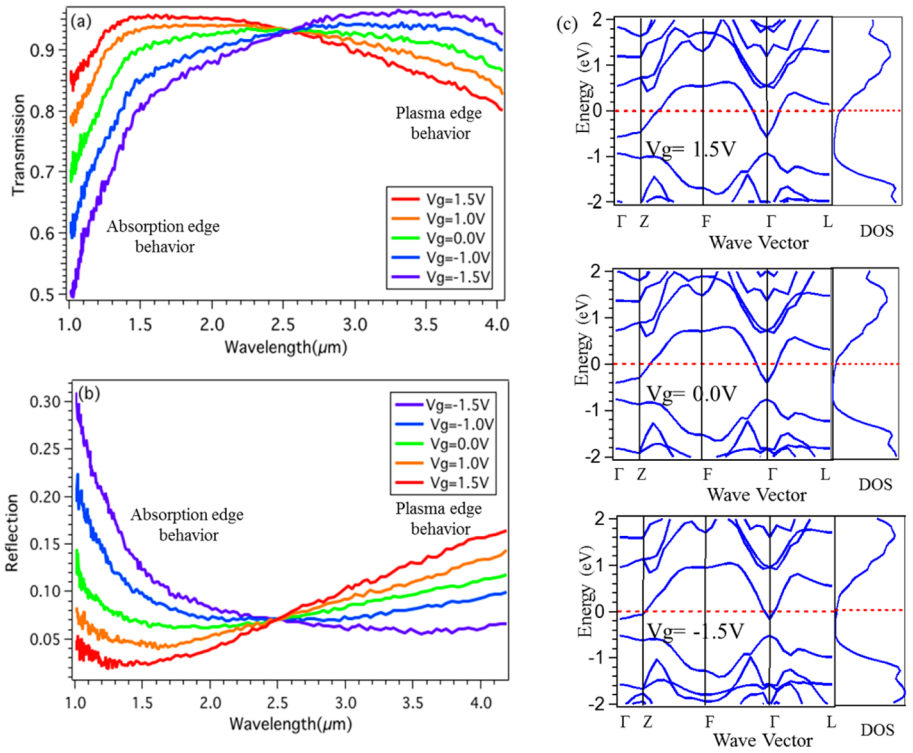

Figure 3. Infrared reflection and transmission of Bi_2Se_3 under EDLG. Optical transmission (a) and reflection (b) spectra of Bi_2Se_3 nanoplates via the EDL gating modulation. The modulated spectra at near-infrared regions exhibits a tunable reflection window, due to the simultaneous modulation of the absorption edge and the electron plasma edge of the nanoplates via the applied EDL gate voltage. (c) Band structure of Bi_2Se_3 nanoplates under positively biased (top) zero-biased (middle), and negatively biased (bottom) EDL gating modulation, based on first-principles density functional theory calculations. The red dashed lines indicate the positions of the Fermi levels.

reflection spectra of a Bi_2Se_3 nanoplate under EDL gating in the near-infrared range. In the optical spectrum, the short wavelength (i.e., $\lambda < 2.5$ μm) absorption edge cutoff corresponds to the fundamental optical gap of the Bi_2Se_3 nanoplates, and the long wavelength (i.e., $\lambda > 2.5$ μm) edge corresponds to the free carrier plasma resonance frequency. To better analyze the experimental results, we plot the transmission and reflection values as a function of the EDL voltage at the fixed wavelengths of $\lambda = 1.5$ μm and $\lambda = 3.5$ μm, as shown in Figure 4a and b, which show that the optical transmission and reflection values depend strongly on the EDL voltage. The figures also show the contrasting behavior between short wavelength $\lambda = 1.5$ μm and long wavelength $\lambda = 3.5$ μm trends. For example, the transmission value increases with increasing EDL voltage at $\lambda = 1.5$ μm, but at long wavelengths the transmission decreases, indicating that there are two optical processes in effect due to the EDL gating modulation.

These trends can be explained with the Drude model, which makes a direct connection between the optical responses of conducting materials and their electronic states. According to this model, the modulated relative permittivity ε can be written as[41]

$$\varepsilon = \varepsilon_\infty - \frac{{\omega_p}^2}{\omega^2 + i\omega\Gamma} = \varepsilon_\infty + \frac{i{\omega_p}^2\tau}{\omega(1 - i\omega\tau)} = \varepsilon_r + i\tilde{\varepsilon_i} = (n + ik)^2 \quad (1)$$

where ε_∞ is the high-frequency dielectric constant, $\Gamma = 1/\tau$ is the damping constant of the free electron plasma, and τ is the relaxation time of the electrons. The plasma resonance frequency is given by $\omega_p^2 = (Ne^2)/(m^*\varepsilon_0)$, where N is the free carrier concentration, m^* is the effective mass of electrons, and n and k are the optical constants which determine the reflection and absorption spectra of the material.

It is worthwhile to consider the Drude model in eq 1 in two limiting cases: low and high frequencies. In the low frequency regime ($\omega\tau \ll 1$), the free carrier term in eq 1 shows a $1/\omega$ dependence as $\omega \to 0$, indicating that this term dominates in the low frequency limit and the material is a perfect reflector at low frequencies. However, in the high frequency response limit ($\omega\tau \gg 1$), the $1/\omega^2$ dependence of the free carrier contribution becomes less important, and other mechanisms will dominate. Thus, at the high frequency limit ($\omega\tau \gg 1$), the free carrier contribution can be neglected, and the material behaves like a dielectric.[42]

In our case ($1 < \omega\tau < \omega_p\tau$), the free carrier contribution plays an important role in the optical properties of Bi_2Se_3. The plasma frequency is the characteristic frequency at which the material changes from a metallic to a dielectric optical response, which occurs at the frequency at which the real part of the relative permittivity vanishes, $\mathrm{Re}(\varepsilon) = 0$. The plasma frequency ($\omega_p^2 = (Ne^2)/(m^*\varepsilon_0)$) is dependent on the free carrier concentration and inversely dependent on the effective mass of the free carriers. The plasma edge of a material refers to the region near its plasma frequency, where its reflectivity increases significantly with increasing incident wavelength.[42] The Drude model predicts that the plasma edge will shift to shorter wavelengths due to a positive EDL modulation of the free carrier concentration.

As shown in Figure 3, the reflection and transmission spectra show a substantial blue shift of the plasma edge induced by the positive EDL modulation. Such behavior provides direct

DOI: 10.1021/acs.nanolett.5b04140
Nano Lett. 2016, 16, 488−496

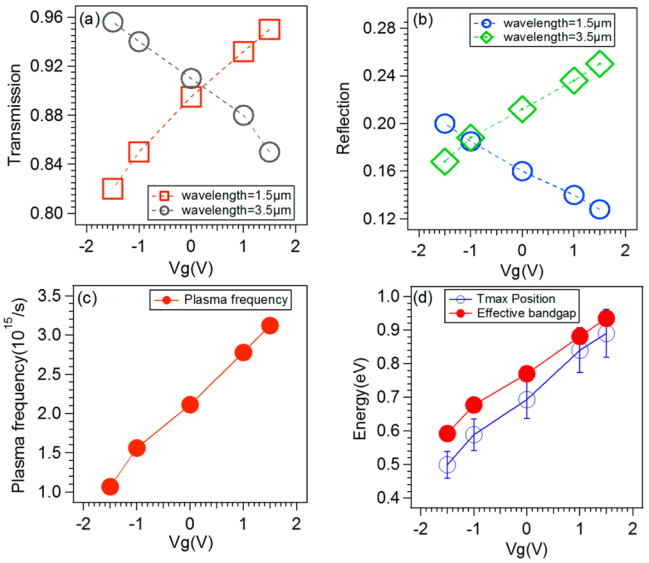

Figure 4. Optical properties of Bi_2Se_3 nanoplates as functions of ILG voltage. Transmission (a) and reflection (b) values of a Bi_2Se_3 nanoplate as functions of the ILG voltage at the short wavelength of λ = 1.5 μm and the long wavelength of λ = 3.5 μm. (c). Plasma frequency extracted from the experimental results based on the Drude model. (d). Experimentally measured onsets of absorption (maximum transmission value) and calculated direct optical transition energies near the Fermi level (effective bandgap) as functions of the ILG voltage. The blue empty circles are the experimentally measured onsets of absorption, and the red solid circles are calculated direct optical transition energies near the gate controlled Fermi level. The increasing effective bandgap is consistent with the observed blue shift of the transmission maximum position.

evidence of the increasing amount of free electrons inside the materials induced by the EDL, which is consistent with the Drude model we described above. We applied the Drude model to our measured results, and it was found to perfectly fit with the experimental data at long wavelengths (Supplementary Figure S4). The value of the plasma frequency can be obtained from the numerical fitting of each curve. As shown in Figure 4c, the plasma frequency is nonlinearly dependent on the EDL voltage due to free electron concentration and effective mass changes induced by the evolution of the Fermi level within the Bi_2Se_3 nanoplates. For example, the plasma frequency reaches $\omega_p = 3.12 \times 10^{15}$/s, with best fit parameters $\varepsilon_\infty = 9.1$ and $\Gamma = 2.1 \times 10^{14}$/s, at the bias voltage $V_G = 1.5V$. The corresponding electron carrier density can be calculated from the plasma frequency,[33,43] which yields an extremely high free electron concentration on the order of 10^{20} cm^{-3}. This level of electron concentration modulation is one of the great advantages of using the EDL gating with 2D material systems. To further study the dynamic optical response of Bi_2Se_3 nanoplates under EDL modulation, we calculate the relative permittivity (ε) of Bi_2Se_3 under the bias of the EDL voltage (seen in Figure S5). Im(ε) dramatically increases with increasing plasma frequency. This is expected from the Drude model when the carrier density is extremely high. Such behavior further confirms the increasing amount of free electrons induced by the EDL inside the materials.

The second effect of the free carrier density modulation is to significantly shift the absorption edge. The absorption edge originates from the onset of optical transitions across the fundamental band gap of a material, which manifests at short wavelengths as a significant increase in the transmission with increasing incident wavelength. The optical modulation behavior of Bi_2Se_3 nanoplates from visible to near-infrared is mainly caused by a substantially altered effective optical bandgap, which is a result of the large free electron concentration modulation in the Bi_2Se_3 nanoplates via EDL gating. This phenomenon is known as the Burstein–Moss shift.[44] As the electron concentration increases, the Fermi level of the material rises into the conduction band, and empty states at the band edge become unavailable. Therefore, optical transitions to the bottom of the conduction band are less likely to occur, resulting in an increased effective bandgap.

For a quantitative study of the correlation between Fermi level shift and EDL voltage, we computed the electronic structure of Bi_2Se_3 using density functional theory (DFT). Assuming EDL gating voltages do not significantly alter the density of states (DOS) shape around the conduction band minimum, we calculated the corresponding Fermi level energy from experimentally derived carrier densities. As shown in Figure 3c, our calculations estimated an increase of the Fermi level energy by 0.34 eV when the bias changes from −1.5 to 1.5 V. It can be seen that, when the EDL is unbiased, the Fermi level is located inside the conduction band due to the heavily n-doped nature of the Bi_2Se_3 nanoplates (middle panel in Figure 3c). While the EDL is positively biased, more electrons will accumulate at the Bi_2Se_3 nanoplate surface, and the increased effective bandgap leads to a blue shift of the absorption edge. A negative bias can lower the Fermi level by reducing the free electron concentration, which frees more low energy optical transitions and shifts the absorption edge to lower energies. This is shown in the near-infrared part of the experimental spectra in Figure 3a and b, providing direct evidence of the optical modulation behavior we observed in the experiments. It is noted that the number of lines in the band structure varies due to subband formation. However, our previous research confirmed that, based on the density of states (DOS) calculation, the energy separation scale in the subbands is too small to affect the optical measurements.[29] The measured onset of the absorption as a function of gate voltage is also shown in Figure 4d. The blue shift of the transmission maximum positions is consistent with the increase in the effective bandgap derived from carrier concentration calculations.

To better demonstrate the universal nature of the EDL technique, we performed similar gating experiments on another layered-structured TMDC material, $MoSe_2$. Dynamic tuning of optical properties was also observed in $MoSe_2$ flakes over similar gating voltages. Modulated transmission spectra of the layered structure $MoSe_2$ flakes (thickness: ~30 nm) in the near-infrared region are shown in Figure 5a and b with an applied positive and negative voltage, respectively. In contrast to the Bi_2Se_3 nanoplates, the Burstein–Moss shift in multilayer $MoSe_2$ involves both electrons (conduction band) and holes (valence band), as illustrated in Figure 5c. The Fermi level is located in the bandgap for lightly n-doped $MoSe_2$ flakes without any bias (middle panel in Figure 5c)[45,46] but lies within the conduction band with a positive gate voltage (top diagram in Figure 5c). On the other hand, when the gate is negatively biased, holes will accumulate in the $MoSe_2$ flakes. The Fermi level will then lie within the valence band (VB) (bottom panel in Figure 5c). The increased free electron (hole) density induced by EDL gating results in moving the Fermi level into the conduction (valence) band. In either case, the effective bandgap will be increased, in contrast to the Bi_2Se_3 behavior. The gating

DOI: 10.1021/acs.nanolett.5b04140
Nano Lett. 2016, 16, 488–496

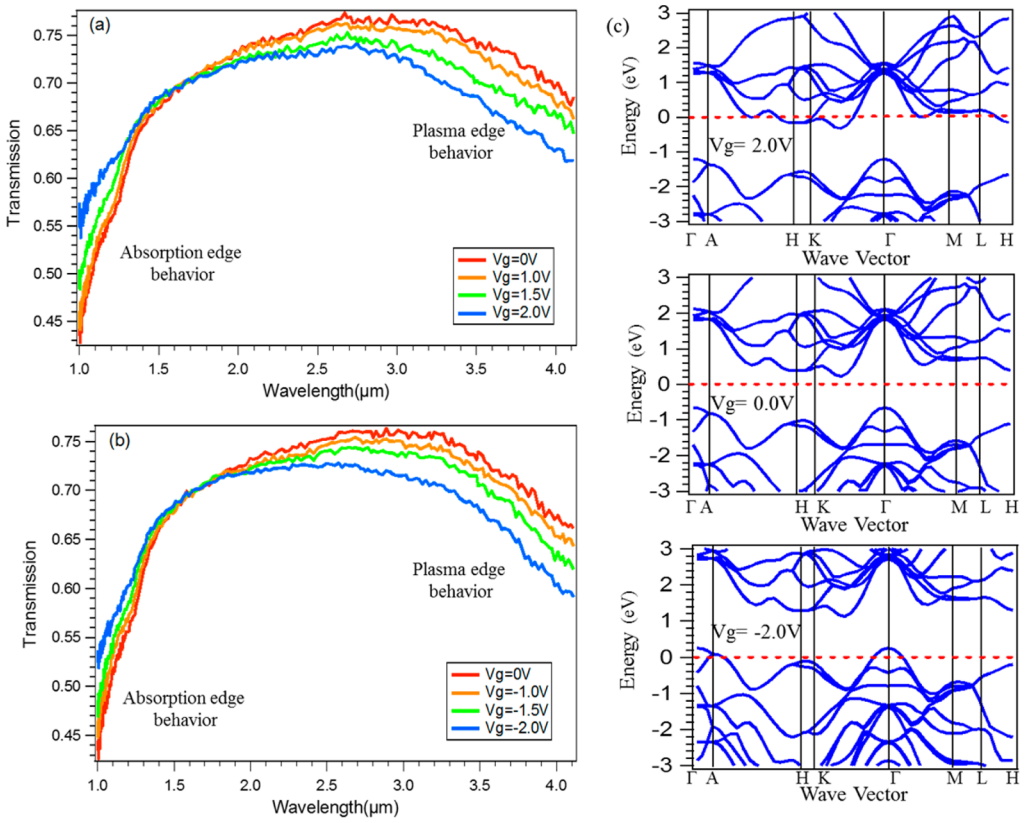

Figure 5. Infrared transmission of $MoSe_2$ under EDLG. Optical transmission spectra of $MoSe_2$ flakes under the applied positive (a) and negative (b) EDL gating modulation. The modulated spectra at near-infrared regions exhibits a similar tunable transmission window as the layered structure Bi_2Se_3 nanoplates, due to the coincident modulation of the absorption edge and the electron and hole plasma edges. (c) Band structure of $MoSe_2$ few layer flakes under positively biased (top) zero-biased (middle), and negatively biased (bottom) EDL gating modulation, based on first-principles density functional theory calculations. The red dashed lines indicate the positions of Fermi levels.

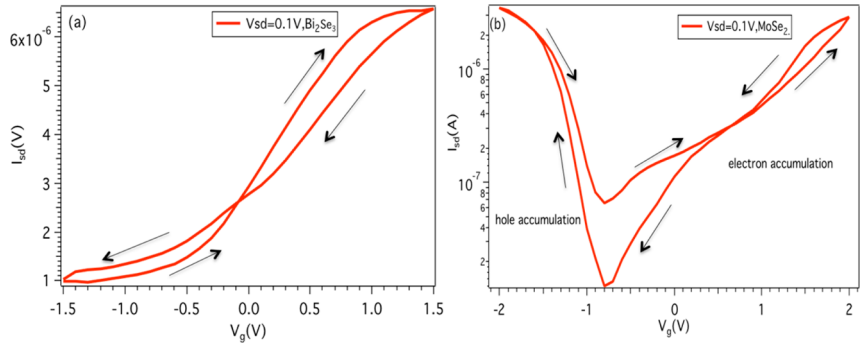

Figure 6. Electronic state change verified by transport measurements. Transport characteristics ($I_{DS} - V_G$) of the Bi_2Se_3 nanoplates (a) and $MoSe_2$ flakes (b) via the EDL gating effect. Compared to $MoSe_2$ flakes, the charge transport behavior indicates a heavily n-doped nature of Bi_2Se_3 nanoplates, such that the Fermi level cannot move into its valence band. The arrows show the direction of the applied voltage sweeps.

induced optical property changes involve the Burstein−Moss shift in either the conduction or valence band, showing a symmetric ambipolar behavior. The observed results indicate that EDL gating can be used to enhance the free carrier concentration to extremely large values in 2D material systems without any chemical reactions. Because of the simultaneous shift of the absorption edge at short wavelengths and the electron plasma edge at long wavelengths via the applied EDL gate voltage, the modulated optical responses of both Bi_2Se_3 and $MoSe_2$ exhibit a tunable transparent spectral window in the infrared to visible range. Since the Fermi level shifts due to EDL gating are much larger than shifts caused by regular chemical doping, this technique creates intense optical modulation over a large wavelength range, including visible wavelengths, which can be used for applications that require tunable optical properties. Such behaviors can be observed in other ILs as well.

As shown in Figure 6a, the electronic state changes that cause the above optical effects were also verified by the transport characteristics, i.e., V_G as a function of the source−drain current (I_{SD}), of the Bi_2Se_3 device with EDL gating at room temperature. With increasing positive V_G, the cations in the EDL accumulate at the top of the thin film surface and induce large amounts of electrons at the Bi_2Se_3 surface, resulting in an intense increase of the I_{SD} from enhanced electron conduction (shown in Figure 6a). Alternatively, on the condition of a

DOI: 10.1021/acs.nanolett.5b04140
Nano Lett. 2016, 16, 488−496

negative bias, electrons are depleted in the nanoplate at the interface, meaning that the I_{SD} decreases due to a lower electron concentration. The electric charge accumulation results in an electric field at the interface, which can be used to tune the Fermi level and the density of electrons in the surface−electron-accumulation layer at the surface of the Bi_2Se_3 samples.[47] Figure 6b shows the transfer characteristics of the $MoSe_2$ flakes under EDL gating at room temperature. A typical ambipolar behavior was observed at room temperature, which is consistent with the lightly n-doped nature of $MoSe_2$ flakes. Multiple samples were measured, and similar transfer characteristics were found in each sample (Supplementary Figure S6), showing high reproducibility.

Conclusion. In summary, we have observed dynamic optical modulation of ultrathin Bi_2Se_3 nanoplates. Dramatic transmission and reflection changes are achieved in nanoplates as thin as 10 nm. Such drastic optical property changes are due to widening of the effective optical band gap enabled by tuning of the electronic states and the E_F of the Bi_2Se_3 samples using EDL gating. A similar dynamic tuning of optical properties in layered-structure $MoSe_2$ further confirms the nature of the optical modulation behavior via the EDL gating technique. The subtle difference in their gating voltage dependence is consistent with the difference of E_F positions inside those two materials. The simultaneous tuning of both absorption edge and plasma edge will lead to potential applications in wide spectral range optical modulators and electrically controlled smart windows. However, currently our devices still operate at relatively low speeds due to the relaxation time for ion motion. In order to overcome the limitation of a low switching rate, further investigations will be needed, such as a dual-gate EDL-FET configuration which may be employed to improve the switching rate in a small tuning range.[48]

Methods. *Solvothermal Synthesis of Bismuth Selenide Nanoplates and Device Fabrication.* Bi_2Se_3 nanoplates were prepared using solvothermal synthesis.[39] Selenium powder (3 mmol, metal basis) and Bi_2O_3 powder (1 mmol, metal basis) were dissolved in ethylene glycol (30 mL), followed by the additions of ethylene diamine tetraacetic acid (EDTA, $(HO_2CCH_2)_2NCH_2CH_2N(CH_2N(CH_2CO_2H)_2$, Alfa Aesar company) powder and high-purity polyvinylpyrrolidone ($PVP,(C_6H_9NO)_n$, Alfa Aesar company). The resulting suspension was sonicated and then sealed in a steel autoclave. Afterward, the autoclave was heated in an oven at a temperature of around 200 °C for 24 h and then gradually cooled to room temperature. The resulting black solution was collected by filtration, washed with ethanol several times, and then dried in a vacuum (10^{-3} Torr) oven at 90 °C. The resulting black power was diluted with ethanol to create a suspension and then deposited on glass substrates using a pipet. The average thickness and lateral size of the nanoplates can be optimized by modifying the concentration of EDTA and temperature. The multilayer $MoSe_2$ flakes were prepared by mechanical exfoliation. The electrical devices were fabricated using photolithography to pattern the electrodes. The nanoplates were then subjected to reactive-ion etching in order to remove any organic residue and surface oxide. E-beam evaporation of 5 nm/100 nm of chromium/gold was used to create the source/drain and gate electrodes. Subsequently, the samples were attached to a chip holder using wire bonding. The thicknesses of the samples were confirmed by AFM measurements, and the thickness of the hexagonal flakes ranged from around 8−22 nm. The chemical identity of the Bi_2Se_3 nanoplates and quality of multiple $MoSe_2$ flakes were confirmed by Raman spectroscopy (Supplementary Figure S2). To confirm the crystallinity of the Bi_2Se_3 nanoplates, we also performed transmission electron microscopy (Supplementary Figure S3).

Optical Transmission, Reflection, and Electric Transport Measurements. Bi_2Se_3 nanoplates were deposited onto glass substrates by drop-casting. All electron transport property measurements were performed in a standard probe station in air at room temperature. Before the electrical measurements, AFM measurements were used to measure the thickness of the Bi_2Se_3 nanoplates and multilayer $MoSe_2$ flakes. We measured their optical transmission images and spectra at visible wavelengths under EDL gating effects using a Nikon Eclipse CI-L and Nikon confocal C1 microscope, respectively. The applied gate voltage was provided by a source meter (Keithley-2400). Reflection and transmission spectra at near-infrared regions were measured using a Bruker Hyperion 2000 infrared microscope and IFS-125/HR Fourier transform infrared spectrometer at room temperature. A transparent knife-edge aperture was used to adjust the beam size such that all of the detected transmitted and reflected light was from the nanoplate sample and not from the nearby substrate. All infrared reflection and transmission results are normalized to the reflection of pure gold and transmission of a bare glass substrate, respectively.

Computational Details. Density functional theory calculations were carried out with the Vienna ab initio software package (VASP),[49] using the projector augmented-wave method[50,51] and the Perdew−Burke−Ernzerhof (PBE) exchange−correlation functional.[52] Electronic band structure and density of state analyses were performed based on static calculations of relaxed structure from the Materials Project[53] with higher *k*-point sampling densities. All data analyses (e.g., band structure, electronic density of state, and carrier concentration analyses) were implemented within the pymatgen python package.[54]

■ ASSOCIATED CONTENT

Supporting Information

The Supporting Information is available free of charge on the ACS Publications website at DOI: 10.1021/acs.nanolett.5b04140.

Detailed information on the Bi_2Se_3 nanoplates synthesis and device fabrication, characterization of the Bi_2Se_3 nanoplates, and details about the numerical calculation of the relative permittivity based on the Drude model (PDF)

■ AUTHOR INFORMATION

Corresponding Author

*E-mail: yaojie@berkeley.edu.

Author Contributions

J.Y. and H.Y. conceived the project. Y.L., X.W., and J.Y. designed the experiment. Y.L. and C.H. prepared the Bi_2Se_3 nanoplates, Y.L., C.K., J.S., and K.T. fabricated the devices. Y.L., X.W., K.T., H.D., and K.A.P. performed DFT calculations and the corresponding analyses, and H.Y. and J.Y. carried out experimental measurements and analyzed the experimental data. All authors contributed to discussions and manuscript revision.

Notes

The authors declare no competing financial interest.

DOI: 10.1021/acs.nanolett.5b04140
Nano Lett. 2016, 16, 488−496

■ ACKNOWLEDGMENTS

Y.L would like to thank Yu Ye for his useful discussions and also Jun Xiao, Sui Yang, Xingchen Quanwei Li, Hanyu Zhu, Qinglin Xia, and Zhiqiang Niu for their experimental assistance. This work is supported by the Samsung Advanced Institute of Technology under the grant 037361-003, and the Hellman Family Foundation. Computational work was supported by the Department of Energy's Basic Energy Sciences program—the Materials Project—under Grant No. EDCBEE, and the Office of Science of the U.S. Department of Energy under Contract No. DEAC02-05CH11231.

■ REFERENCES

(1) Wang, F.; Zhang, Y. B.; Tian, C. S.; Girit, C.; Zettl, A.; Crommie, M.; Shen, Y. R. *Science* **2008**, *320*, 206−209.
(2) Nair, R. R.; Blake, P.; Grigorenko, A. N.; Novoselov, K. S.; Booth, T. J.; Stauber, T.; Peres, N. M. R.; Geim, A. K. *Science* **2008**, *320*, 1308−1308.
(3) Novoselov, K. S.; Geim, A. K.; Morozov, S. V.; Jiang, D.; Zhang, Y.; Dubonos, S. V.; Grigorieva, I. V.; Firsov, A. A. *Science* **2004**, *306*, 666−669.
(4) Chen, C. F.; Park, C. H.; Boudouris, B. W.; Horng, J.; Geng, B. S.; Girit, C.; Zettl, A.; Crommie, M. F.; Segalman, R. A.; Louie, S. G.; Wang, F. *Nature* **2011**, *471*, 617−620.
(5) Seol, J. H.; Jo, I.; Moore, A. L.; Lindsay, L.; Aitken, Z. H.; Pettes, M. T.; Li, X. S.; Yao, Z.; Huang, R.; Broido, D.; Mingo, N.; Ruoff, R. S.; Shi, L. *Science* **2010**, *328*, 213−216.
(6) Zhang, Y. B.; Tan, Y. W.; Stormer, H. L.; Kim, P. *Nature* **2005**, *438*, 201−204.
(7) Arnaud, B.; Lebegue, S.; Rabiller, P.; Alouani, M. *Phys. Rev. Lett.* **2006**, *96*, 026402.
(8) Marom, N.; Bernstein, J.; Garel, J.; Tkatchenko, A.; Joselevich, E.; Kronik, L.; Hod, O. *Phys. Rev. Lett.* **2010**, *105*, 046801.
(9) Ovchinnikov, D.; Allain, A.; Huang, Y. S.; Dumcenco, D.; Kis, A. *ACS Nano* **2014**, *8*, 8174−8181.
(10) Perea-Lopez, N.; Elias, A. L.; Berkdemir, A.; Castro-Beltran, A.; Gutierrez, H. R.; Feng, S. M.; Lv, R. T.; Hayashi, T.; Lopez-Urias, F.; Ghosh, S.; Muchharla, B.; Talapatra, S.; Terrones, H.; Terrones, M. *Adv. Funct. Mater.* **2013**, *23*, 5511−5517.
(11) Ganatra, R.; Zhang, Q. *ACS Nano* **2014**, *8*, 4074−4099.
(12) Late, D. J.; Huang, Y. K.; Liu, B.; Acharya, J.; Shirodkar, S. N.; Luo, J. J.; Yan, A. M.; Charles, D.; Waghmare, U. V.; Dravid, V. P.; Rao, C. N. R. *ACS Nano* **2013**, *7*, 4879−4891.
(13) Torgeson, D. R.; Borsa, F. *Phys. Rev. Lett.* **1976**, *37*, 956−959.
(14) Garvin, J. F.; Morris, R. C. *B Am. Phys. Soc.* **1978**, *23*, 246−246.
(15) Xu, X. D.; Yao, W.; Xiao, D.; Heinz, T. F. *Nat. Phys.* **2014**, *10*, 343−350.
(16) Xia, F. N.; Wang, H.; Xiao, D.; Dubey, M.; Ramasubramaniam, A. *Nat. Photonics* **2014**, *8*, 899−907.
(17) Urbaszek, B.; Marie, X. *Nat. Phys.* **2015**, *11*, 94−95.
(18) Mai, C.; Barrette, A.; Yu, Y. F.; Semenov, Y. G.; Kim, K. W.; Cao, L. Y.; Gundogdu, K. *Nano Lett.* **2014**, *14*, 202−206.
(19) Pumera, M.; Loo, A. H. *TrAC, Trends Anal. Chem.* **2014**, *61*, 49−53.
(20) Yin, X. B.; Ye, Z. L.; Chenet, D. A.; Ye, Y.; O'Brien, K.; Hone, J. C.; Zhang, X. *Science* **2014**, *344*, 488−490.
(21) Wang, Q. H.; Kalantar-Zadeh, K.; Kis, A.; Coleman, J. N.; Strano, M. S. *Nat. Nanotechnol.* **2012**, *7*, 699−712.
(22) Chhowalla, M.; Shin, H. S.; Eda, G.; Li, L. J.; Loh, K. P.; Zhang, H. *Nat. Chem.* **2013**, *5*, 263−275.
(23) Zhang, H. J.; Liu, C. X.; Qi, X. L.; Dai, X.; Fang, Z.; Zhang, S. C. *Nat. Phys.* **2009**, *5*, 438−442.
(24) Neupane, M.; Richardella, A.; Sanchez-Barriga, J.; Xu, S.; Alidoust, N.; Belopolski, I.; Liu, C.; Bian, G.; Zhang, D. M.; Marchenko, D.; Varykhalov, A.; Rader, O.; Leandersson, M.; Balasubramanian, T.; Chang, T. R.; Jeng, H. T.; Basak, S.; Lin, H.; Bansil, A.; Samarth, N.; Hasan, M. Z. *Nat. Commun.* **2014**, *5*, 3841.
(25) Zhang, Y.; He, K.; Chang, C. Z.; Song, C. L.; Wang, L. L.; Chen, X.; Jia, J. F.; Fang, Z.; Dai, X.; Shan, W. Y.; Shen, S. Q.; Niu, Q. A.; Qi, X. L.; Zhang, S. C.; Ma, X. C.; Xue, Q. K. *Nat. Phys.* **2010**, *6*, 584−588.
(26) Liu, Y.; Li, Y. Y.; Rajput, S.; Gilks, D.; Lari, L.; Galindo, P. L.; Weinert, M.; Lazarov, V. K.; Li, L. *Nat. Phys.* **2014**, *10*, 294−299.
(27) Nomura, K.; Koshino, M.; Ryu, S. *Phys. Rev. Lett.* **2007**, *99*, 146806.
(28) Benia, H. M.; Lin, C. T.; Kern, K.; Ast, C. R. *Phys. Rev. Lett.* **2011**, *107*, 177602.
(29) Yao, J.; Koski, K. J.; Luo, W. D.; Cha, J. J.; Hu, L. B.; Kong, D. S.; Narasimhan, V. K.; Huo, K. F.; Cui, Y. *Nat. Commun.* **2014**, *5*, 5670.
(30) Sobota, J. A.; Yang, S. L.; Kemper, A. F.; Lee, J. J.; Schmitt, F. T.; Li, W.; Moore, R. G.; Analytis, J. G.; Fisher, I. R.; Kirchmann, P. S.; Devereaux, T. P.; Shen, Z. X. *Phys. Rev. Lett.* **2013**, *111*, 136802.
(31) Sobota, J. A.; Yang, S.; Analytis, J. G.; Chen, Y. L.; Fisher, I. R.; Kirchmann, P. S.; Shen, Z. X. *Phys. Rev. Lett.* **2012**, *108*, 117403.
(32) Checkelsky, J. G.; Hor, Y. S.; Liu, M. H.; Qu, D. X.; Cava, R. J.; Ong, N. P. *Phys. Rev. Lett.* **2009**, *103*, 246601.
(33) Duan, J. X.; Tang, N.; He, X.; Yan, Y.; Zhang, S.; Qin, X. D.; Wang, X. Q.; Yang, X. L.; Xu, F. J.; Chen, Y. H.; Ge, W. K.; Shen, B. *Sci. Rep.* **2014**, *4*, 4889.
(34) Yuan, H. T.; Shimotani, H.; Tsukazaki, A.; Ohtomo, A.; Kawasaki, M.; Iwasa, Y. *Adv. Funct. Mater.* **2009**, *19*, 1046−1053.
(35) Shimotani, H.; Tsuda, S.; Yuan, H. T.; Yomogida, Y.; Moriya, R.; Takenobu, T.; Yanagi, K.; Iwasa, Y. *Adv. Funct. Mater.* **2014**, *24*, 3305−3311.
(36) Ichimura, T.; Fujiwara, K.; Tanaka, H. *Sci. Rep.* **2014**, *4*, 5818.
(37) Paek, E.; Pak, A. J.; Hwang, G. S. *J. Phys. Chem. C* **2013**, *117*, 23539−23546.
(38) Kasahara, Y.; Nishijima, T.; Sato, T.; Takeuchi, Y.; Ye, J. T.; Yuan, H. T.; Shimotani, H.; Iwasa, Y. *J. Phys. Soc. Jpn.* **2011**, *80*, 022049.
(39) Kong, D. S.; Koski, K. J.; Cha, J. J.; Hong, S. S.; Cui, Y. *Nano Lett.* **2013**, *13*, 632−636.
(40) Zhang, J.; Peng, Z. P.; Soni, A.; Zhao, Y. Y.; Xiong, Y.; Peng, B.; Wang, J. B.; Dresselhaus, M. S.; Xiong, Q. H. *Nano Lett.* **2011**, *11*, 2407−2414.
(41) Yuan, H. T.; Liu, H. W.; Shimotani, H.; Guo, H.; Chen, M. W.; Xue, Q. K.; Iwasa, Y. *Nano Lett.* **2011**, *11*, 2601−2605.
(42) Dresselhaus, G.; Dresselhaus, M. S.; Tauc, J., Eds. *The Optical Properties of Solids*; Academic Press, New York, 1966.
(43) Wang, Z. Y.; Lin, T.; Wei, P.; Liu, X. F.; Dumas, R.; Liu, K.; Shi, J. *Appl. Phys. Lett.* **2010**, *97*, 042112.
(44) Chamlagain, B.; Li, Q.; Ghimire, N. J.; Chuang, H. J.; Perera, M. M.; Tu, H. G.; Xu, Y.; Pan, M. H.; Xiao, D.; Yan, J. Q.; Mandrus, D.; Zhou, Z. X. *ACS Nano* **2014**, *8*, 8710−8710.
(45) Zhang, Y.; Chang, T. R.; Zhou, B.; Cui, Y. T.; Yan, H.; Liu, Z. K.; Schmitt, F.; Lee, J.; Moore, R.; Chen, Y. L.; Lin, H.; Jeng, H. T.; Mo, S. K.; Hussain, Z.; Bansil, A.; Shen, Z. X. *Nat. Nanotechnol.* **2013**, *9*, 111−115.
(46) Ashcroft, N. W.; Mermin, N. D. *Solid State Physics*; Cengage Learning, 1976.
(47) Grundmann, M. *The Physics of Semiconductors: An Introduction Including Devices and Nanophysics*; Springer-Verlag: Berlin, 2006.
(48) Takeya, J.; Yamada, K.; Hara, K.; Shigeto, K.; Tsukagoshi, K.; Ikehata, S.; Aoyagi, Y. *Appl. Phys. Lett.* **2006**, *88*, 112102.
(49) Kresse, G.; Hafner, J. *Phys. Rev. B: Condens. Matter Mater. Phys.* **1993**, *47*, 558.
(50) Blochl, P. E. *Phys. Rev. B: Condens. Matter Mater. Phys.* **1994**, *50*, 17953.
(51) Kresse, G.; Joubert, D. *Phys. Rev. B: Condens. Matter Mater. Phys.* **1999**, *59*, 1758.
(52) Perdew, J. P.; Burke, K.; Ernzerhof, M. *Phys. Rev. Lett.* **1996**, *77*, 3865−68.
(53) Jain, A.; Ong, S. P.; Hautier, G.; Chen, W.; Richards, W. D.; Dacek, S.; Cholia, S.; Gunter, D.; Skinner, D.; Ceder, G.; Persson, K. A. *APL Mater.* **2013**, *1*, 011002.

DOI: 10.1021/acs.nanolett.5b04140
Nano Lett. 2016, 16, 488−496

(54) Ong, S. P.; Richards, W. D.; Jain, A.; Hautier, G.; Kocher, M.; Cholia, S.; Gunter, D.; Chevrier, V. L.; Persson, K. A.; Ceder, G. *Comput. Mater. Sci.* **2013**, *68*, 314−319.

DOI: 10.1021/acs.nanolett.5b04140
Nano Lett. 2016, 16, 488−496